

## MATRYOSKA HOLES: NESTED EMISSION RINGS IN THE TRANSITIONAL DISK OPH IRS 48

J.M. BROWN<sup>1</sup>, K.A. ROSENFELD<sup>1</sup>, S.M. ANDREWS<sup>1</sup>, D.J. WILNER<sup>1</sup>, E.F. VAN DISHOCK<sup>2,3</sup>

*To appear in ApJ*

### ABSTRACT

The processes that form transition disks - disks with depleted inner regions - are not well understood; possible scenarios include planet formation, grain growth and photoevaporation. Disks with spatially resolved dust holes are rare, but, in general, even less is known about the gas structure. The disk surrounding the A0 star Oph IRS 48 in the nearby  $\rho$  Ophiuchus region has a 30 AU radius hole previously detected in the 18.7  $\mu\text{m}$  dust continuum and in warm CO in the 5  $\mu\text{m}$  fundamental rovibrational band. We present here Submillimeter Array 880  $\mu\text{m}$  continuum imaging resolving an inner hole. However, the radius of the hole in the millimeter dust is only 13 AU, significantly smaller than measured at other wavelengths. The nesting structure of the disk is counter-intuitive, with increasingly large radii rings of emission seen in the millimeter dust ( $12.9^{+1.7}_{-3.4}$  AU), 5  $\mu\text{m}$  CO (30 AU) and 18.7  $\mu\text{m}$  dust (peaking at 55 AU). We discuss possible explanations for this structure, including self-shadowing that cools the disk surface layers, photodissociation of CO, and photoevaporation. However, understanding this unusual disk within the stringent multi-wavelength spatial constraints will require further observations to search for cold atomic and molecular gas.

*Subject headings:* stars: pre-main-sequence — (stars:) planetary systems: protoplanetary disks — stars:individual:Oph IRS 48 — planetary systems: formation – submillimeter

### 1. INTRODUCTION

Understanding the interplay between dust and gas is crucial for determining the evolutionary pathways of protoplanetary disks. Gas dominates the mass and dynamics of the disk, but dust is both easier to trace observationally and contributes directly to planet core formation. Models predict that massive planets clear their orbital paths, creating distinctive gaps in their natal disks (Crida & Morbidelli 2007; Bryden et al. 1999; Artymowicz & Lubow 1994). Transition disks, characterized by observed dust deficits in the inner regions, may be the result of this process (e.g. Strom et al. 1989; Calvet et al. 2002; Brown et al. 2007; Najita et al. 2007). The recent discoveries of young substellar candidates in the transition disks T Cha and LkCa 15 lend credence to this hypothesis (Huélamo et al. 2011; Kraus & Ireland 2012). However, processes other than orbital clearing can potentially cause dust deficits, including photoevaporation and grain growth. The gas distribution could be diagnostic of different scenarios. In disk photoevaporation models, the dust is tied to the gas resulting in similar distributions and timescales (Alexander et al. 2006; Owen et al. 2011). In contrast, grain growth to very large sizes would result in an apparent dust hole but no drop in the gas density. Finally, stellar and planetary companions present an intermediate case with some movement of gas across the gaps into the inner disk expected depending on companion mass and location (Artymowicz & Lubow 1996; Zhu et al. 2011). The presence of gaps can enhance other

disk clearing mechanisms such as the magneto-rotational instability (Chiang & Murray-Clay 2007) and photoevaporation (Alexander & Armitage 2009). Knowledge of the gas distribution is also particularly relevant for studying young planets as the gas drives both formation and migration.

The A0 star IRS 48 in the  $\rho$  Ophiuchi star formation region ( $\sim 1$  Myr, Luhman & Rieke 1999; 121 pc, Loinard et al. 2008) has an unusual disk. Spatially resolved 18.7  $\mu\text{m}$  imaging of the dust continuum revealed a ring-like structure with a peak-to-peak diameter of 110 AU and a central hole with a radius of  $\sim 30$  AU (Geers et al. 2007). Strong polycyclic aromatic hydrocarbon (PAH) emission, commonly a tracer of gaseous molecular material, was unresolved and centered on the stellar position, interior to the ring seen in the 18.7  $\mu\text{m}$  dust. The CO gas might be expected to follow the PAH distribution and thus be located inside the dust hole. However, resolved imaging with the VLT-CRIRES showed warm CO emission in a 30 AU radius ring, coincident with the proposed dust hole wall (Brown et al. 2012). The presence of PAHs was explained by their longer survival time relative to CO in high UV flux, low density regions. Brown et al. (2012) suggest that truncation of the gas and dust, as might be caused by a planet, lowers the density in the inner region leading to photodissociation of CO interior to the truncation radius. This scenario should lead to a dust hole detectable with millimeter interferometry.

Millimeter imaging of transitional disks provides some of the best constraints on cavity size and characteristics. Resolving the cavities requires both long baselines and good (u, v) coverage to achieve the necessary high spatial resolution and dynamic range. The optically thin emission observed in the submillimeter is very sensitive to the mass surface density profile. However, spatially resolved studies have been restricted to the brightest

<sup>1</sup> Harvard-Smithsonian Center for Astrophysics, 60 Garden St., MS 78, Cambridge, MA 02138; jannabrown@cfa.harvard.edu

<sup>2</sup> Leiden Observatory, P.O. Box 9513, NL-2300 RA Leiden, The Netherlands

<sup>3</sup> Max-Planck-Institut für extraterrestrische Physik, Postfach 1312, 85741 Garching, Germany

disks. Despite improving statistics, only a limited number of transition disks have been observed at the spatial scales necessary to resolve the inner cavity (Piétu et al. 2006, Hughes et al. 2007, 2009, Brown et al. 2008, 2009, Andrews et al. 2009, 2011b).

We present in this paper Submillimeter Array (SMA) 880  $\mu\text{m}$  imaging showing a hole in the distribution of large dust grains in the disk around Oph IRS 48. However, surprisingly, the size of the millimeter dust hole is significantly smaller than that observed in the 18.7  $\mu\text{m}$  dust and 5  $\mu\text{m}$  gas. We discuss the observations (§2), the models used to determine the hole size (§3) and finally discuss the implications of the millimeter data and some theories as to the cause of the discrepancy (§4).

## 2. OBSERVATIONS AND RESULTS

We observed Oph IRS 48 (WLY 2-48) with the Submillimeter Array (SMA) in the very extended configuration at 345 GHz (880  $\mu\text{m}$ ). Two tracks were obtained with eight antennas on 2011 August 29 and five antennas on 2011 August 26. The position measured by the SMA was  $\alpha = 16^{\text{h}}27^{\text{m}}37^{\text{s}}.17$ ,  $\delta = -24^{\circ}30'35''.5$ , J2000. Baseline lengths ranged from 30 to 590 m. The beam size was  $0''.45$  by  $0''.24$  arcsec at a position angle of  $27.4^{\circ}$ . Double sideband (DSB) receivers tuned to 341.165 GHz provided 4 GHz of bandwidth per sideband. The visibility phases were calibrated using the quasars J1625-254 (1.4 Jy) and J1626-298 (0.8 Jy), with 10 minute cycles. 3C454.3 was used for passband calibration. The absolute flux scale was calibrated from a measurement of Neptune from the same night. The uncertainty in the flux scale is estimated to be 15%.

Figure 1 presents the image (left) and visibilities (right). While the image is clearly not centrally peaked, we focus the analysis on the visibilities where a null more clearly defines the structure change. Sharp transitions in the mass surface density, such as a hole, are seen in aperture synthesis observations as a null in the flux distribution with (u,v) distance (e.g., Andrews et al. 2011b). In contrast, most classical T Tauri stars have power-law mass surface density profiles, resulting in a smooth decline of flux with (u,v) distance. Another advantage of visibility domain analysis is a better understanding of the uncertainties, due to the lack of additional image processing, including Fourier transformation and non-linear deconvolution. The visibilities in Figure 1 were deprojected to account for position angle, PA, and disk inclination,  $i$ , and binned assuming a circular disk (e.g., Hughes et al. 2007). The deprojected (u,v) distance is  $R = \sqrt{d_a^2 + d_b^2}$  with  $d_a = R \sin \phi$  and  $d_b = R \cos \phi \cos i$  where  $\phi = \arctan(v/u) - \text{PA}$ .

Earlier archival data from 2007 May 14 observed IRS 48 at 230 GHz (1.3 mm) in the very extended configuration. The track had only 6 working antennas and a beam size of  $0''.67 \times 0''.4$  (P.A. =  $-7.8^{\circ}$ ). The spatial resolution was inadequate to clearly resolve the millimeter dust hole, but the data indicated that the millimeter dust was unlikely to follow the shorter wavelength emission. The visibilities are overlaid in gray on Figure 1 but all further analysis uses the higher spatial resolution 880  $\mu\text{m}$  data.

Spatial filtering of flux from the outer disk beyond  $\sim 100$  AU is a concern with the long baselines in the SMA data. IRS 48 has been observed with single dish millime-

ter telescopes with a flux of  $180 \pm 9$  mJy with JCMT-SCUBA at 860  $\mu\text{m}$  (Andrews & Williams 2007) and  $60 \pm 10$  mJy with the IRAM 30m at 1.3 mm (Motte et al. 1998). The SMA tracks have total fluxes of 160 mJy at 880  $\mu\text{m}$  and 50 mJy at 1.3 mm. Less than 20% of the total flux has thus been lost in the interferometric data, ruling out the possibility of a large reservoir of outer disk millimeter dust.

## 3. MODELING

We model the millimeter emission following the similarity solution approach which has been used to characterize the millimeter dust in both normal and transition disks (Hughes et al. 2008; Andrews et al. 2009, 2011a,b). Our emission model is taken to be azimuthally symmetric with a surface brightness profile appropriate for optically thin thermal emission,

$$I_\nu \propto B_\nu(T_d)(1 - e^{-\tau}) \approx B_\nu(T_d)\tau \quad (1)$$

where  $B_\nu$  is the Planck function,  $T_d$  is the dust temperature, and  $\tau$  is the optical depth. The dust temperature is assumed to follow a power-law profile normalized by the stellar temperature of IRS 48:

$$T_d = T_* \left(\frac{r}{r_*}\right)^{-0.5} \quad (2)$$

where  $T_* = 9000$  K and  $r_* = 1.35 R_\odot$ . The optical depth across the disk is set by the surface density for which we adopt the similarity solution appropriate for a viscous accretion disk (Lynden-Bell & Pringle 1974; Hartmann et al. 1998):

$$\tau \propto \left(\frac{r}{r_c}\right)^{-\gamma} \exp\left[-\left(\frac{r}{r_c}\right)^{2-\gamma}\right] \quad (3)$$

where  $\gamma$  sets the gradient of the profile and  $r_c$  is the characteristic scaling radius. We include a cavity by setting to zero any emission within its radius,  $R_{\text{cav}}$ .

After normalizing and projecting the model image onto the sky plane with some inclination, position angle, and positional offsets, we use MIRIAD to sample the model visibilities. The position angle is fixed to  $90^{\circ}$  based on the shorter wavelength data. The fitness of each model, or the likelihood, is constructed from the chi-squared statistic assuming the visibilities have uncorrelated, Gaussian errors,  $\mathcal{L} \propto \exp(-\chi^2/2)$ . To estimate the best fit model parameters and their associated uncertainties, we sample the posterior distribution using an ensemble MCMC algorithm (Goodman & Weare 2010; Foreman-Mackey et al. 2012). We report the best fit parameters and the uncertainties from the 68% confidence intervals of the marginalized distribution (Table 1). The best fit model image and visibility fits are shown in Fig. 1.

We also explored a couple of alternate models to understand the constraints the data put on the millimeter dust distribution. First, a constant density ring model required flux between 7 and 48 AU to match the visibilities. Second,  $R_{\text{cav}}$  was fixed at 30 AU to match the warm CO gas ring (Brown et al. 2012) and a constant density of dust was introduced interior to  $R_{\text{cav}}$ . This model still required 50% of the millimeter flux to come from within  $R_{\text{cav}}$ . In both cases, the fit produced looked adequate by

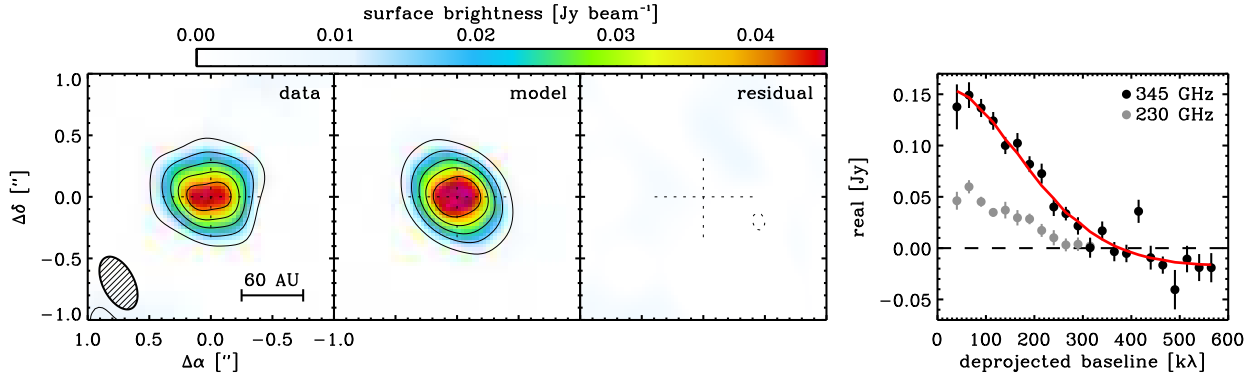


FIG. 1.— Images of the data (left), model (center left) and residuals (center right). The contours are  $3\sigma$  intervals where the RMS noise is 2.7 mJy/beam. The (u,v) visibilities for 345 GHz (black) and 230 GHz (gray) are on the far right with the best fit model from Table 1 in red.

TABLE 1  
MODEL PARAMETERS

Parameter	Best fit	Lower bound	Upper bound
$F_{880\mu\text{m}}$ (Jy)	0.16	0.150	0.165
$r_c$ (AU)	35	27	36
$\gamma$	0.12	-0.49	0.6
$R_{\text{cav}}$ (AU)	12.9	9.5	14.6
Inclination ( $^\circ$ )	35	28	38

eye but had a larger  $\chi^2$  than the similarity solution fit reported in Table 1. The implication is that, regardless of model details, both a central dropoff in the millimeter emission and substantial dust within the  $5\ \mu\text{m}$  CO ring are required.

Both the  $18.7\ \mu\text{m}$  and CO images show asymmetries with the north side brighter than the south. However, the millimeter image shows no significant asymmetries beyond those expected from an inclined disk. The asymmetries at shorter wavelengths may reflect variable extinction of the illuminating radiation field.

The derived inclination of  $35^\circ$  is smaller than those calculated from the  $5\ \mu\text{m}$  CO ( $42^\circ \pm 6^\circ$ ) and the  $18.7\ \mu\text{m}$  dust ( $48^\circ \pm 8^\circ$ ). The inclination was left as a free parameter in the similarity solution models with lower inclinations resulting in a smoother visibility profile and smaller  $\chi^2$ . This could be the result of azimuthal averaging over asymmetric structure that is unseen at the SMA resolution. Large inclinations result in a slightly larger central cavity in the millimeter dust with  $45^\circ$  corresponding to a best fit cavity size of 15 AU.

#### 4. DISCUSSION

Oph IRS 48 is well-studied with resolved measurements of the disk and central hole at several wavelengths and, unusually, constraints on both the gas and dust. Despite spatially resolved rings of emission in the  $18.7\ \mu\text{m}$  dust (55 AU peak; Geers et al. 2007) and the  $5\ \mu\text{m}$  CO (30 AU peak; Brown et al. 2012), the inner edge of the millimeter dust lies interior to both, with a cutoff in the dust density at the even smaller radius of  $12.9^{+1.7}_{-3.4}$  AU (Fig. 2). The SMA image definitively rules out the millimeter emission following the structure in either the  $5\ \mu\text{m}$  CO or the  $18.7\ \mu\text{m}$  dust. The central hole is barely resolved with the SMA with a large portion of flux within the central beam. Thus, all models require a significant per-

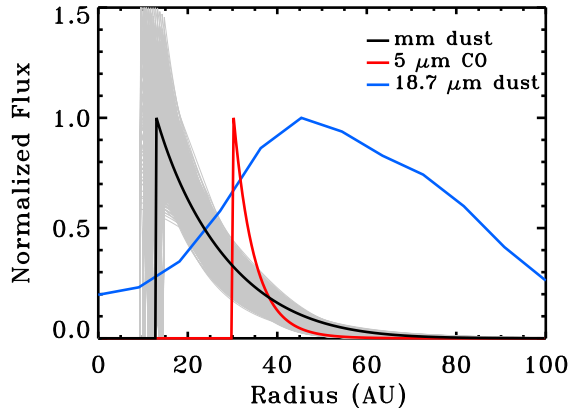


FIG. 2.— The radial distribution of flux from the millimeter dust (black),  $5\ \mu\text{m}$  CO (red) and  $18.7\ \mu\text{m}$  dust (blue). The millimeter profile is the best fit profile listed in Table 1 with the grey region representing fits within the error bars. The  $5\ \mu\text{m}$  CO profile is the best fit model from Brown et al. (2012) Figure 8. The  $18.7\ \mu\text{m}$  dust flux is a cut along the major axis of the Geers et al. (2007) VISIR image after 2-D maximum likelihood deconvolution of the PSF.

centage of the millimeter flux to come from within the CO and IR dust rings. If the disk is currently forming planets, the complex disk structure may provide regions advantageous to planet and planetesimal formation. It may be the case that already formed planets are responsible for some of the sculpting seen in the disk.

Both infrared measurements likely trace only the surface layers of the disk. The VLT-CRIRES  $5\ \mu\text{m}$  CO observations are very sensitive to warm CO with constraints both spatially and spectrally. However, the data are less sensitive to cold CO and completely insensitive to non-molecular gas or other species of molecular gas. The VISIR  $18.7\ \mu\text{m}$  image has a PSF of  $\sim 0''.5$  which is similar to the CO hole size. The  $18.7\ \mu\text{m}$  dust hole may be larger than the 30 AU previously reported (Geers et al. 2007) as seen in the deconvolved cut in Figure 2 (noted also by Maaskant et al., in prep; Bruderer et al., 2011, priv. comm.). While the majority of the  $18.7\ \mu\text{m}$  emission is from outside the millimeter dust, the inner regions may not be entirely void of infrared emitting dust.

The millimeter dust emission places some constraints

on the amount of gas within the hole under assumptions of a canonical gas to dust ratio. In the best fit model, 71% of the millimeter flux arises from dust within the 30 AU radius gas ring. From all the models, 40-90 % of the millimeter emission must be interior to 30 AU. We use the Beckwith et al. (1990) conversion of millimeter flux to disk mass with a  $\beta$  of 1 (Rodmann et al. 2006). The dust temperature is taken to be in the range of 50-150 K. The gas mass within the 30 AU CO ring is then  $10^{-4}$  -  $10^{-3} M_{\odot}$  corresponding to a CO mass of  $10^{-7}$ - $10^{-6} M_{\odot}$ , assuming a  $H_2/CO$  number ratio of  $10^4$ . In a flared disk with a scale height set to the hydrostatic pressure at 200 K, the density of CO is  $10^6$ - $10^7 \text{ cm}^{-3}$  or a surface density of  $10^{19}$ - $10^{20} \text{ cm}^{-2}$ , comparable to a disk with no cavity. Significantly warmer gas is likely to produce  $5 \mu\text{m}$  CO emission detectable in the CRIRES data.

There are three basic scenarios to reconcile the millimeter dust and  $5 \mu\text{m}$  CO emission: 1.) the gas (and dust) is cold and therefore not detectable in the infrared, 2.) the CO is photodissociated and only atomic gas is left interior to 30 AU, or 3.) the gas has been removed leaving millimeter dust and PAHs.

#### 4.1. Scenario 1

Shadowing from a puffed up inner rim, either at the millimeter dust wall or from atomic gas or PAHs closer to the star, could cool the surface layers of the disk further out. The  $5 \mu\text{m}$  CO limits the amount of warm gas within the 30 AU gas radius but the limits are much less stringent at cooler temperatures (Brown et al. 2012, their Figure 12). A temperature of  $\sim 150$  K or less throughout the inner disk is needed to reconcile the  $5 \mu\text{m}$  CO surface density limit with the modeled millimeter surface density, assuming a gas-to-dust ratio of 100. Any illuminated wall would also likely need to be devoid of CO. The shadowing region would require a large scale height to shadow the disk out to 30 AU. In order for this scenario to be plausible, the inner regions must be very settled while the outer structure is flared, exposing the surface layers to stellar radiation to produce the infrared emission.

#### 4.2. Scenario 2

Strong enough UV fields can photodissociate CO, with the photodissociation rate in an unattenuated interstellar field being  $2 \times 10^{-10} \text{ s}^{-1}$ . The UV field around an A0 star such as IRS 48 is much stronger than the interstellar field even in the critical 912-1100 Å range and would lead to a photodissociation lifetime of  $< 1$  year. However, CO photodissociation is subject to self-shielding with the lines becoming saturated at a  $^{12}\text{CO}$  column density of about  $10^{15} \text{ cm}^{-2}$ , strongly decreasing the photodissociation rate (van Dishoeck & Black 1988; Visser et al. 2009). Both millimeter dust grains and PAH molecules are also effective absorbers of UV radiation, lowering the UV field strength and thus the photodissociation rate. The estimated CO density based on the millimeter dust would be strongly self-shielding making complete photodissociation unlikely.

#### 4.3. Scenario 3

Removal of only the gas within 30 AU resulting in a strongly decreased gas-to-dust ratio is a final possibility.

Photoevaporation primarily affects the gas with small dust grains tied to the gas flow. It may be possible for large enough dust grains to remain. Destructive collisions of the remaining large particles would then be needed to generate the PAHs also seen from the inner regions.

These different scenarios should leave differing observational traces which further observations may be able to distinguish. In the case of cold CO, ALMA observations will have the sensitivity and spatial resolution to look for cold CO within the central region of the disk. For photodissociated CO, optical spectroastrometric or high spectral resolution submillimeter observations of atomic C or O would determine if the photodissociation products of CO are present within 30 AU. If the gas is removed completely, neither cold CO nor the atomic components of CO would be present in the inner disk region.

The ring of  $18.7 \mu\text{m}$  dust is even more difficult to understand with most of the emission coming from outside either the millimeter dust or the  $5 \mu\text{m}$  CO. The dominant  $18.7 \mu\text{m}$  flux from  $\sim 55$  AU has no obvious counterpart in the millimeter emission. Like the  $5 \mu\text{m}$  CO, the  $18.7 \mu\text{m}$  flux comes from the disk surface and could reflect differences in illumination and heating of the surface layers rather than underlying changes in the distribution. However, the centrally-peaked PAH emission points to some heating and small particles in the inner region. Recent studies in the mid-IR and scattered light suggest that small surface particles within the cavities seen in larger grains are common (Muto et al. 2012; Dong et al. 2012). Holes visible in the mid-IR are often of similar size to those seen in the submillimeter (e.g. Panic et al. 2012; Thalmann et al. 2010). However, the scattered light profiles, tracing the small surface grains, are smooth with no decrease within the cavity. Dust filtration or trapping creating grain size differences across planetary gaps has been proposed (Rice et al. 2006; Pinilla et al. 2012), with the largest particles left on the outside of the gap and smaller particles, being more closely tied to the gas, allowed closer to the star. While the mid-IR dust and PAHs in Oph IRS 48 may fit this paradigm, the large millimeter dust interior to the smaller mid-IR emitting dust does not. Likewise,  $5 \mu\text{m}$  CO emission usually arises interior to submillimeter holes rather than from further out in disk (Salyk et al. 2009; Pontoppidan et al. 2008). Continued multiwavelength studies are vital to search for other examples of the inside-out nesting structure seen in the Oph IRS 48 disk.

## 5. CONCLUSIONS

We have used new spatially resolved SMA  $880 \mu\text{m}$  observations to place stringent constraints of the dust distribution within the Oph IRS 48 disk. The SMA data clearly rules out that the millimeter dust distribution following either the  $5 \mu\text{m}$  CO or  $18.7 \mu\text{m}$  dust. A large fraction of the millimeter flux is from dust interior to both the  $18.7 \mu\text{m}$  dust ring (55 AU radius) and the  $5 \mu\text{m}$  CO emission (30 AU radius). The millimeter dust also shows a strong drop in surface density with a null in the visibilities. Our similarity solution models place the hole at  $12.9^{+1.7}_{-3.4}$  AU. The millimeter emission clearly shows that an empty cavity is not responsible for the CO

gas ring described in Brown et al. (2012). Further observations are needed to distinguish between the potential scenarios of cold shadowed gas, photodissociated CO and low gas-to-dust ratio, but all these scenarios result in an unusual environment for potential planet formation.

The Submillimeter Array is a joint project between the Smithsonian Astrophysical Observatory and the Academia Sinica Institute of Astronomy and Astro-

physics and is funded by the Smithsonian Institution and the Academia Sinica. The authors thank Jes Jorgensen for providing the earlier 230 GHz data and Vincent Geers for the reduced VISIR data. J.M. Brown acknowledges the Smithsonian Astrophysical Observatory for support from a SMA fellowship. Astrochemistry at Leiden is supported by a Spinoza grant from the Netherlands Organization for Scientific Research (NWO) and by EU A-ERC grant 291141 CHEMPLAN. Facilities: SMA

## REFERENCES

- Alexander, R. D. & Armitage, P. J. 2009, *ApJ*, 704, 989  
 Alexander, R. D., Clarke, C. J., & Pringle, J. E. 2006, *MNRAS*, 369, 229  
 Andrews, S. M., Rosenfeld, K. A., Wilner, D. J., & Bremer, M. 2011a, *ApJ*, 742, L5  
 Andrews, S. M. & Williams, J. P. 2007, *ApJ*, 671, 1800  
 Andrews, S. M., Wilner, D. J., Espaillat, C., Hughes, A. M., Dullemond, C. P., McClure, M. K., Qi, C., & Brown, J. M. 2011b, *ApJ*, 732, 42  
 Andrews, S. M., Wilner, D. J., Hughes, A. M., Qi, C., & Dullemond, C. P. 2009, *ApJ*, 700, 1502  
 Artymowicz, P. & Lubow, S. H. 1994, *ApJ*, 421, 651  
 —. 1996, *ApJ*, 467, L77+  
 Beckwith, S. V. W., Sargent, A. I., Chini, R. S., & Guesten, R. 1990, *AJ*, 99, 924  
 Brown, J. M., Blake, G. A., Dullemond, C. P., Merín, B., Augereau, J. C., Boogert, A. C. A., Evans, II, N. J., Geers, V. C., Lahuis, F., Kessler-Silacci, J. E., Pontoppidan, K. M., & van Dishoeck, E. F. 2007, *ApJ*, 664, L107  
 Brown, J. M., Blake, G. A., Qi, C., Dullemond, C. P., & Wilner, D. J. 2008, *ApJ*, 675, L109  
 Brown, J. M., Blake, G. A., Qi, C., Dullemond, C. P., Wilner, D. J., & Williams, J. P. 2009, *ApJ*, 704, 496  
 Brown, J. M., Herczeg, G. J., Pontoppidan, K. M., & van Dishoeck, E. F. 2012, *ApJ*, 744, 116  
 Bryden, G., Chen, X., Lin, D. N. C., Nelson, R. P., & Papaloizou, J. C. B. 1999, *ApJ*, 514, 344  
 Calvet, N., D'Alessio, P., Hartmann, L., Wilner, D., Walsh, A., & Sitko, M. 2002, *ApJ*, 568, 1008  
 Chiang, E. & Murray-Clay, R. 2007, *Nature Physics*, 3, 604  
 Crida, A. & Morbidelli, A. 2007, *MNRAS*, 377, 1324  
 Dong, R. et al. 2012, *ApJ*, 750, 161  
 Foreman-Mackey, D., Hogg, D. W., Lang, D., & Goodman, J. 2012, *ArXiv e-prints*  
 Geers, V. C., Pontoppidan, K. M., van Dishoeck, E. F., Dullemond, C. P., Augereau, J.-C., Merín, B., Oliveira, I., & Pel, J. W. 2007, *A&A*, 469, L35  
 Goodman, J. & Weare, J. 2010, *Comm. App. Math. Comp. Sci*, 5, 65  
 Hartmann, L., Calvet, N., Gullbring, E., & D'Alessio, P. 1998, *ApJ*, 495, 385  
 Huélamo, N., Lacour, S., Tuthill, P., Ireland, M., Kraus, A., & Chauvin, G. 2011, *A&A*, 528, L7+  
 Hughes, A. M., Andrews, S. M., Espaillat, C., Wilner, D. J., Calvet, N., D'Alessio, P., Qi, C., Williams, J. P., & Hogerheijde, M. R. 2009, *ApJ*, 698, 131  
 Hughes, A. M., Wilner, D. J., Calvet, N., D'Alessio, P., Claussen, M. J., & Hogerheijde, M. R. 2007, *ApJ*, 664, 536  
 Hughes, A. M., Wilner, D. J., Qi, C., & Hogerheijde, M. R. 2008, *ApJ*, 678, 1119  
 Kraus, A. L. & Ireland, M. J. 2012, *ApJ*, 745, 5  
 Loinard, L., Torres, R. M., Mioduszewski, A. J., & Rodríguez, L. F. 2008, *ApJ*, 675, L29  
 Luhman, K. L. & Rieke, G. H. 1999, *ApJ*, 525, 440  
 Lynden-Bell, D. & Pringle, J. E. 1974, *MNRAS*, 168, 603  
 Motte, F., Andre, P., & Neri, R. 1998, *A&A*, 336, 150  
 Muto, T. et al. 2012, *ApJ*, 748, L22  
 Najita, J. R., Strom, S. E., & Muzerolle, J. 2007, *MNRAS*, 378, 369  
 Owen, J. E., Ercolano, B., & Clarke, C. J. 2011, *MNRAS*, 412, 13  
 Panic, O., Ratzka, T., Mulders, G. D., Dominik, C., van Boekel, R., Henning, T., Jaffe, W., & Min, M. 2012, *ArXiv e-prints*  
 Piétu, V., Dutrey, A., Guilloteau, S., Chapillon, E., & Pety, J. 2006, *A&A*, 460, L43  
 Pinilla, P., Benisty, M., & Birnstiel, T. 2012, *ArXiv e-prints*  
 Pontoppidan, K. M., Blake, G. A., van Dishoeck, E. F., Smette, A., Ireland, M. J., & Brown, J. 2008, *ApJ*, 684, 1323  
 Rice, W. K. M., Armitage, P. J., Wood, K., & Lodato, G. 2006, *MNRAS*, 373, 1619  
 Rodmann, J., Henning, T., Chandler, C. J., Mundy, L. G., & Wilner, D. J. 2006, *A&A*, 446, 211  
 Salyk, C., Blake, G. A., Boogert, A. C. A., & Brown, J. M. 2009, *ApJ*, 699, 330  
 Strom, K. M., Strom, S. E., Edwards, S., Cabrit, S., & Skrutskie, M. F. 1989, *AJ*, 97, 1451  
 Thalmann, C. et al. 2010, *ApJ*, 718, L87  
 van Dishoeck, E. F. & Black, J. H. 1988, *ApJ*, 334, 771  
 Visser, R., van Dishoeck, E. F., & Black, J. H. 2009, *A&A*, 503, 323  
 Zhu, Z., Nelson, R. P., Hartmann, L., Espaillat, C., & Calvet, N. 2011, *ApJ*, 729, 47